

# Supporting Information for: Validity of approximated expressions for electro-osmotic flow in nanopores evaluated by continuum electrohydrodynamics and atomistic simulations

Giovanni Di Muccio<sup>a</sup>, Domingo Francesco Iacoviello<sup>b</sup>, Simone Gargano<sup>b</sup>, Blasco Morozzo della Rocca<sup>c</sup>, Mauro Chinappi<sup>b,\*</sup>

<sup>a</sup>*Dipartimento di Scienze della Vita e dell'Ambiente, Università Politecnica dell Marche, Via Brecce Bianche, 60131 Ancona, Italia*

<sup>b</sup>*Dipartimento di Ingegneria Industriale, Università di Roma Tor Vergata, via del politecnico 1, 00133, Roma, Italia and*

<sup>c</sup>*Dipartimento di Biologia, Università di Roma Tor Vergata, via della ricerca scientifica, 00133, Roma, Italia*

Email: mauro.chinappi@uniroma2.it

Supplementary Note S1: Classical derivation of Goldman-Hodgkin-Katz equation	p. S-2
Supplementary Note S2: Details of the MD protocol	p. S-5
Supplementary Figure S1: Membrane model for GHK	p. S-3
Supplementary Figure S2: Boundary conditions for PNP-S	p. S-7
Supplementary Figure S3: Geometries and computational meshes	p. S-8
Supplementary Figure S4: PNP-S convergence tests	p. S-9
Supplementary Figure S5: Additional data on current and reversal potential from PNP-S simulations	p. S-10
Supplementary Figure S6: MD Data on solid state nanopores	p. S-11
Supplementary Figure S7: PNP-S simulations in cylindrical nanopores	p. S-12
Supplementary Figure S8: Additional PNP-S data	p. S-13
Supplementary Figure S9: Additional data, EOF vs pore length	p. S-14
Supplementary Table S1: Ion and electroosmotic current for PNP-S simulations	p. S-15
Supplementary Table S2: Ion and electroosmotic current for solid state nanopores (MD)	p. S-15
Supplementary Table S3: Additional data for solid state nanopores (MD)	p. S-16
Supplementary Table S4: Ion and electroosmotic current for biological nanopores (MD)	p. S-16
Supplementary References	p. S-17

**SUPPLEMENTARY NOTE S1: CLASSICAL DERIVATION OF  
GOLDMAN-HODGKIN-KATZ EQUATION**

Here, for reader benefit, we report the standard derivation of the Goldman-Hodgkin-Katz (GHK) equation [S1, S2]. We suggest the interested readers to explore also the interesting discussion in [S3].

**1D model of flux through a membrane.** The membrane is modelled as a homogeneous slab of thickness  $L$  and the problem is 1D, *i.e.* all the quantities depends only on the coordinate normal to the membrane,  $z$  in our reference system, see Fig. (S1). The problem is assumed to be stationary. The  $z$ -component of the flux of the  $i$ -th ionic species is the sum of a diffusion and an electrophoretic contribution and it is written as

$$J_i = -D_i \frac{dc_i}{dz} + c_i e \nu_i \mu_i E_z, \quad (\text{S1})$$

where  $D_i$  is the diffusion coefficient of the  $i$ -th species in the membrane,  $\mu_i = D_i/k_B T$  its mobility with  $k_B$  the Boltzmann constant and  $T$  the temperature,  $\nu_i$  the valence,  $e$  the elementary charge and  $E_z = dV/dz$  the  $z$ -component of the electric field with  $V$  the electric potential. The electric field is assumed to be constant through the membrane, so, with the sign convention reported in Fig. (S1),  $E_z = \Delta V/L$ . Eq. (S1) is valid in the membrane and the reservoir conditions (that, in a real system, are set far from the membrane) are used as boundary conditions at  $z = 0$  (*trans*) and  $z = L$  (*cis*).

Eq. (S1), equipped with the above mentioned boundary conditions, can be directly integrated between  $z = 0$  and  $z = L$  providing the following expression for the ion flux

$$J_i = e \nu_i \mu_i E_z \frac{C_i^c - C_i^t \exp(e \nu_i \beta \Delta V)}{1 - \exp(e \nu_i \beta \Delta V)}, \quad (\text{S2})$$

with, as usual,  $\beta = 1/k_B T$ . Note that, in our reference system, fluxes through the membrane are positive when going from *trans* to *cis* reservoir. If concentrations at the two reservoirs are identical,

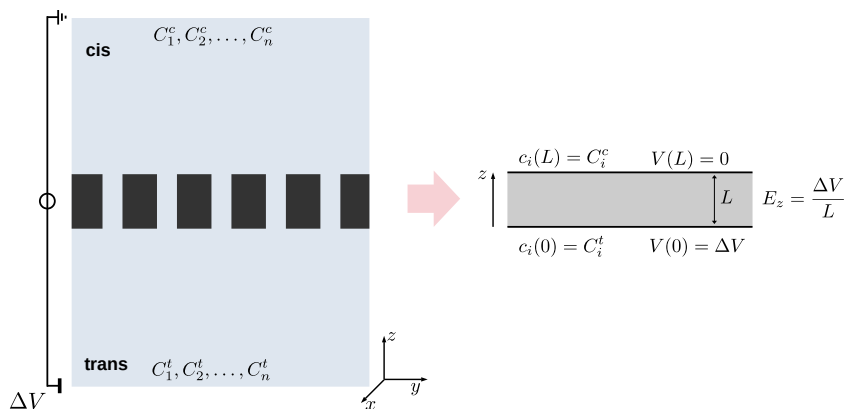


**FIG. S1. Membrane model.** A membrane separates two reservoirs (*cis* and *trans*) where two electrolyte solutions are present. Concentration of dissolved ions are indicated as  $C_i^{c/t}$ , where the superscript  $c/t$  refer to the *cis* of *trans* reservoir and the subscript  $i$  to the ion species. A voltage  $\Delta V$  is applied. Without loss of generality, we assume that the *cis* reservoir is grounded. The membrane contains nanopores that allow the passage of ions and water. In the Goldman description [S1], the system is model as a uniform membrane and the reservoir conditions are applied to the membrane boundary. Moreover, as a further simplification, the electric field inside the membrane is assumed to be uniform, so that,  $E_z = \Delta V/L$ .

the flux is only ruled by electrophoresis, and, thus, Eq. (S2), reduces to  $J_i = c_i e \nu_i \mu_i E_z$ . If, instead,  $\Delta V \rightarrow 0$ , the flux is only diffusive and Eq. (S2) – applying, for instance, the de l'Hôpital rule – reduces to  $J_i = D_i (C_i^t - C_i^c) / L$ . In summary, for small  $\Delta C$  and  $\Delta V$ , the flux reads

$$J_i = D_i \frac{\Delta C_i}{L} + c_i e \nu_i \mu_i \frac{\Delta V}{L} . \quad (\text{S3})$$

Concerning the voltage, the linear approximation is valid for  $\Delta V \ll k_B T / e$ , that for  $T = 300\text{K}$  implies  $\Delta V \ll 25\text{ mV}$ . Note that in Eq. (S3) the coefficients that multiply  $\Delta C$  and  $\Delta V$  are positive coherently with our definition for  $\Delta C$  and  $\Delta V$  and reference system. In different manuscripts, authors can make different choices (for instance, one can invert the ground electrode), hence, before applying formulas like Eq. (S3), it is important to understand which convention is used.

**Reversal potential.** The total ionic current can be obtained from ionic fluxes as

$$I = A \sum_i^{N_s} e \nu_i J_i , \quad (\text{S4})$$

with  $A$  the area of the membrane and  $N_s$  is the number of ionic species.  $I$  is a function of the applied voltage  $\Delta V$  and the ionic concentration in the two reservoirs ( $C_i^{c/t}$ ). In experiments, the curve  $I(\Delta V)$  can be measured while the individual contributions  $J_i$  are not accessible. For a given set of concentrations  $C_i^{c/t}$ , the voltage  $V_r$  for which  $I = 0$  is indicated as the reversal potential. Given the reversal potential  $V_r$ , it is possible to deduce some property of the membrane. In this theoretical framework, usually, a parameter called permeability is defined as

$$P_i = \frac{D_i}{L} = \frac{\mu_i k_B T}{L} , \quad (\text{S5})$$

where, in the last expression, the fluctuation-dissipation relation  $D_i = \mu_i k_B T$  is used. So, the total current can be rewritten as

$$I = A \sum_i^{N_s} e^2 \nu_i^2 P_i \beta \Delta V \frac{C_i^c - C_i^t \exp(e \nu_i \beta \Delta V)}{1 - \exp(e \nu_i \beta \Delta V)} . \quad (\text{S6})$$

When  $I = 0$ , Eq. (S6) provides a relation between the permeabilities  $P_i$  and the reversal potential  $\Delta V = V_r$ . This implies, that, even if the 1D theoretical approach used to derive GHK is build on assumptions that are not valid in a real membrane (for instance, the diffusion coefficient  $D_i$  is not a measurable quantity, the membrane thickness  $L$  may be not homogeneous, the diffusion in the reservoirs and the entrance effects on the pores are not considered) it allows, in principle, to directly measure an effective quantity (the permeability  $P_i$ ) or, at least, to measure the relation between the permeabilities of different ions.

The individual flux in Eq. (S2) and its linear approximation can be rewritten as function of the permeability as it follows

$$J_i = e \nu_i P_i \frac{\Delta V}{k_B T} \frac{C_i^c - C_i^t \exp(e \nu_i \beta \Delta V)}{1 - \exp(e \nu_i \beta \Delta V)} , \quad (\text{S7})$$

$$J_i = P_i \Delta C_i + e \nu_i P_i C_i \frac{\Delta V}{k_B T} , \quad (\text{S8})$$

where, for small  $\Delta C$ , we have  $C_i^t \simeq C_i^c \equiv C_i$ . The small forcing approximation (S8) is extremely useful since it allows to straightforwardly estimate  $P_i$  from simple simulation set-ups. For instance, in atomistic simulations it is very common to apply an voltage  $\Delta V$  and measure the individual flux of ions (for  $\Delta C = 0$ ) while in continuum PNP-S simulations (see Methods in the main text) it is possible to modify both  $\Delta C$  and  $\Delta V$ , by altering the boundary conditions far from the membrane.

**The case of a 1:1 electrolyte.** In several nanopore experiments, the solution is a 1:1 electrolyte, as KCl or NaCl [S4]. In this condition, (S6) reduces to

$$I = e^2 P_+ \beta \Delta V \frac{C_+^c - C_+^t \exp(e\beta \Delta V)}{1 - \exp(e\beta \Delta V)} + e^2 P_- \beta \Delta V \frac{C_-^c - C_-^t \exp(-e\beta \Delta V)}{1 - \exp(-e\beta \Delta V)}, \quad (\text{S9})$$

that, for  $I = 0$ , provides a relation between the reversal potential  $V_r$  and the ratio of permeabilities  $P_+/P_-$  as it follows

$$V_r = \frac{k_B T}{e} \log \frac{P_+ C_+^c + P_- C_-^t}{P_+ C_+^t + P_- C_-^c}. \quad (\text{S10})$$

that, solved for the permeability ratio gives

$$\frac{P_+}{P_-} = \frac{C_-^t - C_-^c \exp(e\beta V_r)}{C_+^t \exp(e\beta V_r) - C_+^c}. \quad (\text{S11})$$

Eq. (S11) is commonly used in nanopore papers as a measure of the anion/cation selectivity of the pore [S5–S8].

## SUPPLEMENTARY NOTE S2: DETAILS OF THE MD PROTOCOL

**Molecular Dynamics Simulation Methods.** All the MD runs were carried out using NAMD 2.14 [S9] with a time step  $\Delta t = 2.0$  fs, unless otherwise stated. Particle mesh Ewald [S10] method with a 1.0 Å spaced grid are used for long-range electrostatic interactions. The force field is CHARMM36 [S11] with TIP3P model for water [S12] and CUFIX corrections for ions [S13]. A cutoff of 12 Å (switching distance of 10 Å) was used for the short-range nonbonded interactions. Periodic boundary conditions with a parallelepipedic box are used. A Langevin thermostat was used for all the simulations while a Nosé–Hoover Langevin piston pressure control was used for constant pressure simulations [S14].

**Biological pore and membrane set-up and equilibration.** The protocol used to build and to equilibrate the system is similar to the one reported in Di Muccio et al. [S15] that is also similar to the one used in previous works [S16, S17]. The CytK structure is the same used in [S18]. For MspA, we used the structure (PDB:1UUN, [S19] downloaded from the OPM database [S20] so that the pore axis is already aligned with the z-axis. For CsgG we used PDB:4UV3 [S21], and we modelled the  $\beta$ -barrel missing fragments (F144, F193 to L199) by using the SWISS-MODEL server [S22]. Mutants were obtained by using VMD mutator plugin [S23]. A POPC bilayer membrane, parallel to the x-y plane, was generated using VMD [S23]. Before the equilibration, the lipid molecules overlapping the protein or located in the pore lumen were removed. Subsequently, water and ions were added using the solvate and ionize VMD plugins. After minimization, a first equilibration step ( $P = 1$  atm flexible cell, constant ratio,  $T = 300$  K, time step  $\Delta t = 0.5$  fs) is performed, to allow the relaxation of lipid tails and of the electrolyte. External forces were applied to the water molecules to avoid their penetration into the membrane. The  $C\alpha$ s of the pore were kept fixed and the lipid heads were harmonically constrained to their z-positions (spring constant  $k = 1$  kcal/(mol Å<sup>2</sup>)), allowing a movement along the x-y plane. An initial temperature ramp is imposed (every 5 ps the velocities are rescaled to a temperature of 0, 25, 50, . . . , 275, 300 K) for a smoothly relaxation of the system. The total duration of this first step is  $\simeq 250$  ps with minor differences among the simulations. A second equilibration run was performed where the lipid heads were harmonically constrained only to their x-y position. Protein  $C\alpha$ s were still fixed. Pressure and temperature controls were used as in the first step, as well as the time step. The total duration of this second step is  $250 \simeq ps$ . In a third, 1 ns long (time step 1 fs), equilibration step, all the constraints on the membrane are removed. All the other control settings were as in the previous step. The last equilibration step is an NPT run of 1 ns (time step 1 fs) with no constraints on the lipids and no external forces to keep the water molecules out of the membrane. No constraints on the membrane and on the protein are applied.

**Solid state nanopores.** The protocol used to build and to equilibrate the system is similar to the one employed in [S8]. We remand to that manuscript for details.

**Non-equilibrium run and ionic and water current estimation.** An electrical field  $\mathbf{E} = (0, 0, E_z)$ , with  $E_z = \Delta V/L_z$ , with  $\Delta V$  the applied voltage and  $L_z$  the length of the periodic box along the z-axis, is applied. The ionic current was measured via the equation [S15, S24]:

$$I(t) = \frac{1}{\Delta t L_z} \sum_{i=1}^N q_i [z_i(t + \Delta t) - z_i(t)], \quad (\text{S12})$$

in which  $I(t)$  is the average ionic current in the interval  $(t, t + \Delta t)$ ,  $q_i$  is the charge of ion  $i$ ,  $z_i$  is the displacement of ion  $i$  on the z-axis during the interval  $\Delta t$ . The sum is over all ions. Cation and

anion currents are calculated limiting Eq. (S12) to only one ionic species, while for EOF the sum is over the Oxygen of the water molecules with  $q_i = 1$ . Absolute errors and confidence intervals were calculated through block average.

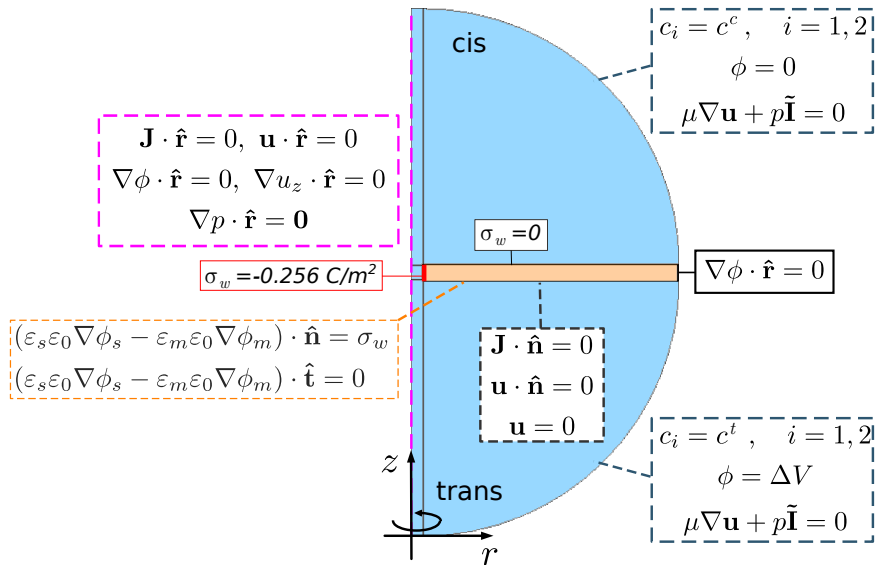


FIG. S2. **Boundary conditions for PNP-S.** Here the system with pore radius  $d = 2 \text{ nm}$  and  $L = 1.4 \text{ nm}$ , one of the different geometries simulated, is considered as example, in order to illustrate the boundary conditions for the PNP-S problem. The nanopore is obtained from a membrane of thickness  $L$  and relative permittivity of  $\epsilon_m = 6$ . The membrane boundary is neutral, while the pore surface is negatively charged with a surface charge density  $\sigma_w$ . This charge density is imposed through the condition:  $(\epsilon_s \epsilon_0 \nabla \phi_s - \epsilon_m \epsilon_0 \nabla \phi_m) \cdot \hat{\mathbf{n}} = \sigma_w$ , where the  $\phi_s$  and  $\phi_m$  indicate the potential inside the fluid and membrane, respectively. Also, since the surface charge does not affect the electric field in the tangential direction across the solid-fluid interface, the following condition is also imposed:  $(\epsilon_s \epsilon_0 \nabla \phi_s - \epsilon_m \epsilon_0 \nabla \phi_m) \cdot \hat{\mathbf{t}} = 0$ . For clarity, we used this notation only for this boundary condition since the potential that appears in the Poisson equation is not divided in those two terms, thus hereinafter the potential is simply indicated with  $\phi$ . The impermeability conditions for the membrane is  $\mathbf{J} \cdot \hat{\mathbf{n}} = 0$  and the no-slip condition is considered  $\mathbf{u} = 0$ . In the spherical reservoirs, of radius  $r_s = 15L$  (with  $L$  function of the pore radius), the concentration of each ionic species is fixed at  $c_i = C^c$  at the cis reservoir and  $c_i = C^t$  for the trans one. We supposed also that the active electrode is immersed in the trans reservoir and, therefore, here the potential at the boundary of the right reservoir is set to  $\phi = \Delta V$ , while in the left one  $\phi = 0$ . Since no mechanical forces exert an action on the system, the free stress condition  $\mu \nabla \mathbf{u} + p \tilde{\mathbf{I}} = 0$  is used, where  $\tilde{\mathbf{I}}$  is the identity matrix. The boundary conditions are the same employed in [S8, S25], for a more complete discussion see, among others [S26].

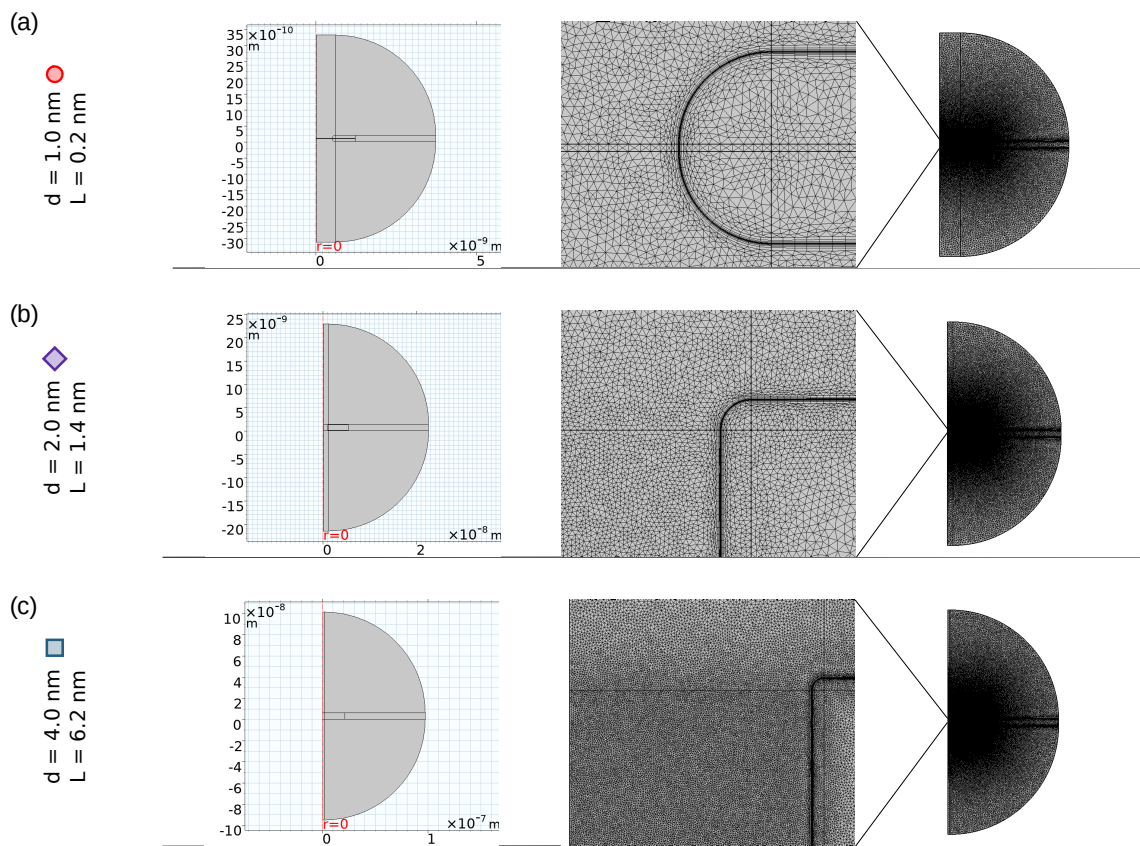


FIG. S3. **Geometries and computational meshes**, used in Poisson-Nernst-Planck-Stokes (PNP-S) nanofluidic simulations for evaluating electro-osmotic flow (EOF) through nanopores. Each geometry corresponds to a distinct pore size and length configuration used in the continuum electrohydrodynamics, the same of the atomistic simulations of Fig. 3 of the main text. The first column show the system geometries and size, the second a zoom of the third column, representing the mesh used to discretize the PNP-S equations. Pores size are reported on the left: (a) Diameter  $d = 1.0$  nm, Length  $L = 0.2$  nm; (b) Diameter  $d = 2.0$  nm, Length  $L = 1.4$  nm; (c) Diameter  $d = 4.0$  nm, Length  $L = 6.2$  nm.

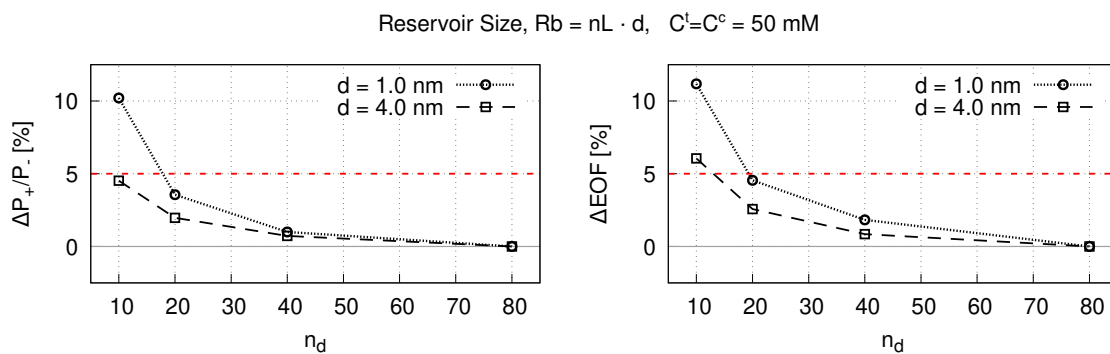
Reservoir Variation, **Convergence Test**

FIG. S4. **Test for numerical convergence with increasing reservoir size.** In experiment, the voltage and the concentration differences are applied very far from the membrane. This condition cannot be efficiently reproduced in simulations. Consequently, it is relevant to verify how the result changes with the size of the reservoir. In the Figure,  $n_d$  is the radius of the hemispherical reservoir expressed in terms of pore diameters.

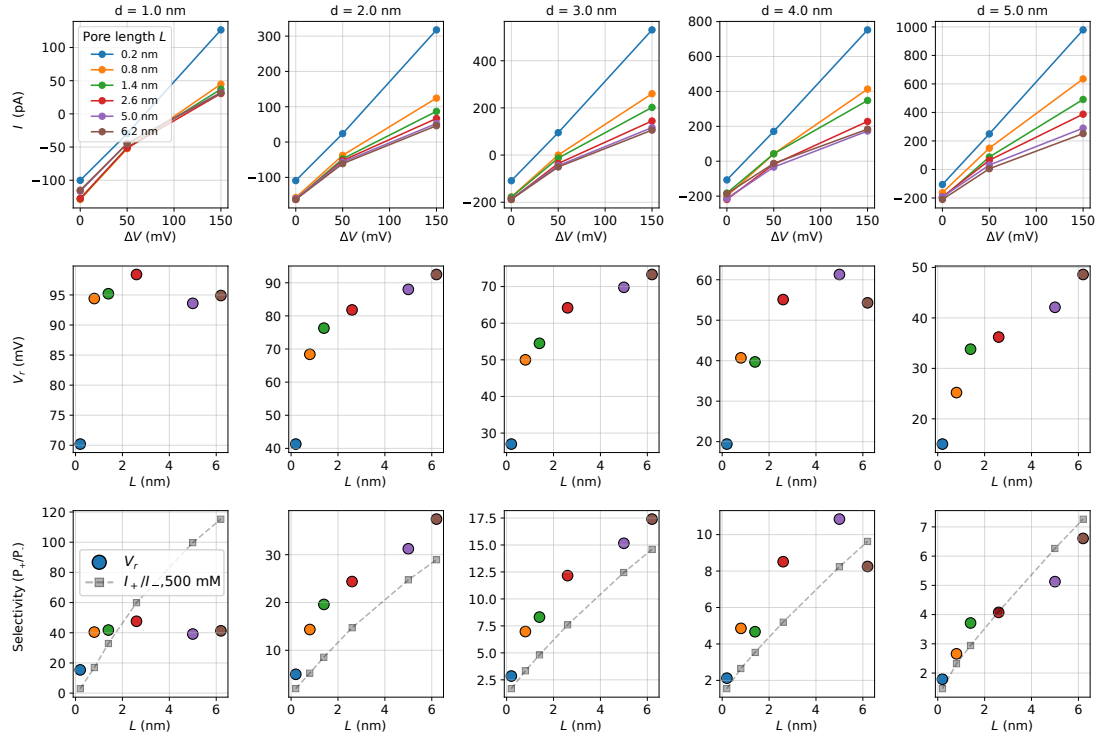


FIG. S5. **Additional data on current  $I$  and reversal potential  $V_r$  from PNP-S simulations.** The general setup is shown in Fig. 2a of the main text, with  $C^c = 500$  mM and  $C^t = 5$  mM. (Top row) Total ionic current  $I$  versus applied voltage ( $\Delta V = 0, 50, 150$  mV) for five pore diameters ( $d = 1.0, 2.0, 3.0, 4.0, 5.0$  nm). Each curve in a panel corresponds to a different pore length  $L$ , see inset in top-left panel. (Middle row) Reversal potential  $V_r$  as a function of  $L$ . (Bottom row) Permeability ratio from Eq. (4) of the manuscript as a function of  $L$ . Gray squares is the permeability ratio from simulations where the two reservoirs are both at  $c_0 = 500$  mM. Points in the middle and bottom rows are color-coded by pore diameter, matching the top-row panels. Data for the simulated currents and flows are reported on Zenodo, doi:10.5281/zenodo.14916088.

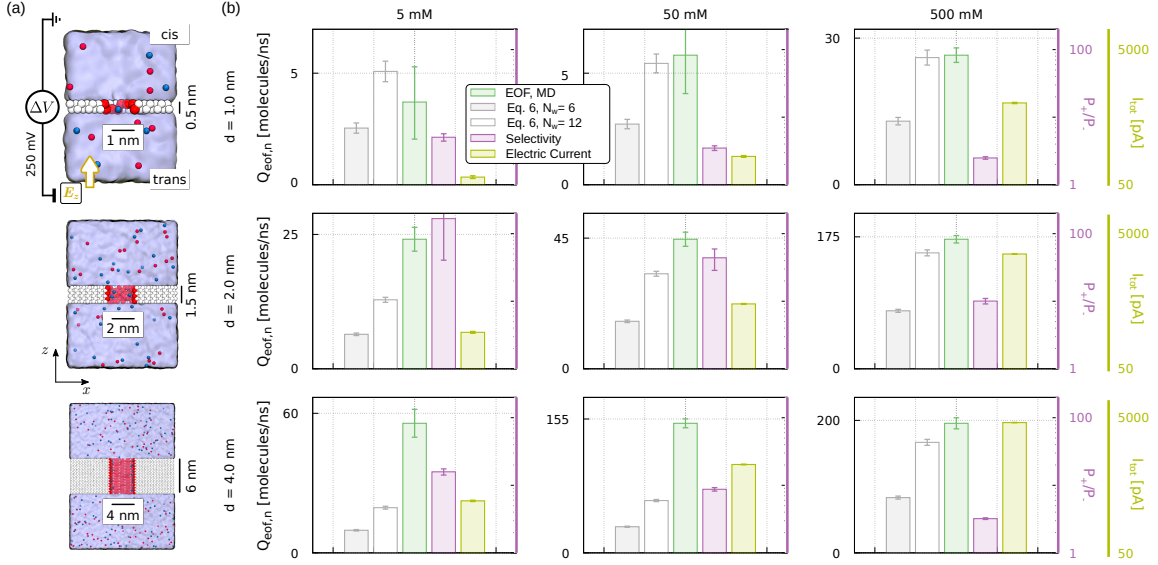


FIG. S6. Atomistic simulation of EOF through a solid state nanopores. (a) Set-up of atomistic simulation for three systems, having different pore diameters and lengths. The pores are made of Lennard-Jones atoms, represented as VdW spheres, white for the uncharged atoms and red for the charged ones. The red spheres carry a charge corresponding to an average surface charge of  $-0.256 \text{ C/m}^2$ . (b) EOF, selectivity and total electric current from MD simulations for the cation selective pores displayed on the left, for different concentrations, measured under an electric field  $E_z$  corresponding to a transmembrane voltage of 250 mV. The prediction from the Gu et al. [S5] theory, Eq. (6) of the manuscript, obtained using the cation and anion currents from MD and  $N_w = 6$  or  $N_w = 12$  are reported in gray and white. For each system, averages are obtained from 400 ns simulations. Confidence intervals were obtained using a block average with each block corresponding to 10 ns. For derived quantities (such as selectivity) we applied uncertainty propagation rules. For the [S5] prediction, we used Eq. (6) instead of Eq. (10) to reduce the error propagation. To compact multiple data on the same plot, three different scales are used for the vertical axis: a linear scale for  $Q_{eo,n}$ , a logarithmic scale for  $P_+/P_-$  and a logarithmic scale for the total current. For completeness, the original data are reported in table S2 of the supporting information.

**Comment:** The narrowest pore ( $d = 1.0 \text{ nm}$ ) at 500 mM KCl, is selective for cations with  $P_+/P_- \simeq 2.5$ . The cation selectivity is associated with a EOF that, for  $\Delta V = 250 \text{ mV}$  amounts to  $Q_{eo,n} \simeq 26 \text{ molecules/ns}$ . The parameter  $N_w$  represents the number of water molecules that are dragged by a single ion. Using  $N_w = 12$ , we get  $Q_{eo,n} \simeq 24$  that is quite close to the MD value, while, using  $N_w = 6$  the prediction is quite far from MD. A similar agreement is present at  $C = 50 \text{ mM KCl}$  and  $C = 5 \text{ mM KCl}$  indicating, that, at least in the case of very narrow pores, the Gu et al. argument can provide a good estimate of the EOF. Instead, increasing the diameter of the pore, the scenario changes. For both  $d = 2 \text{ nm}$  and  $d = 4 \text{ nm}$ , at 0.5 M KCl Eq. 6 with  $N_w = 12$  follows the MD trends while for smaller concentration strong deviations from MD are evident. Overall the MD data is always larger than the prediction (even using  $N_w = 12$ , a quite high value for the number of water molecules in the coordination shell of an ion) and, in some cases, the errors can reach a factor of 2 or 3, in particular for larger pores. The MD data allow to explore other features of the selectivity and EOF in nanopores. For instance, the permeability ratio  $P_+/P_-$  is larger at smaller ion concentration, as it is expected since the Debye layer is thicker. Another observation, in line with the theoretical expectation, is the trend of the total current  $I$  with ion concentration. As expected,  $I$  increases with the concentration, however, the increase is not linear as it would be for large pores but sub-linear, i.e.,  $I$  at 500 nM for  $d = 4 \text{ nm}$  is only 4 times larger than  $I$  at 50 nM. This effect is due to the relevance of surface contribution at the nanoscale with respect to the bulk ones. Indeed, the fixed surface charge at the pore wall brings a number of counterions in the pore that is roughly independent on the ion concentration. The same geometries were also simulated with PNP-S, see Figures S7 and S8.

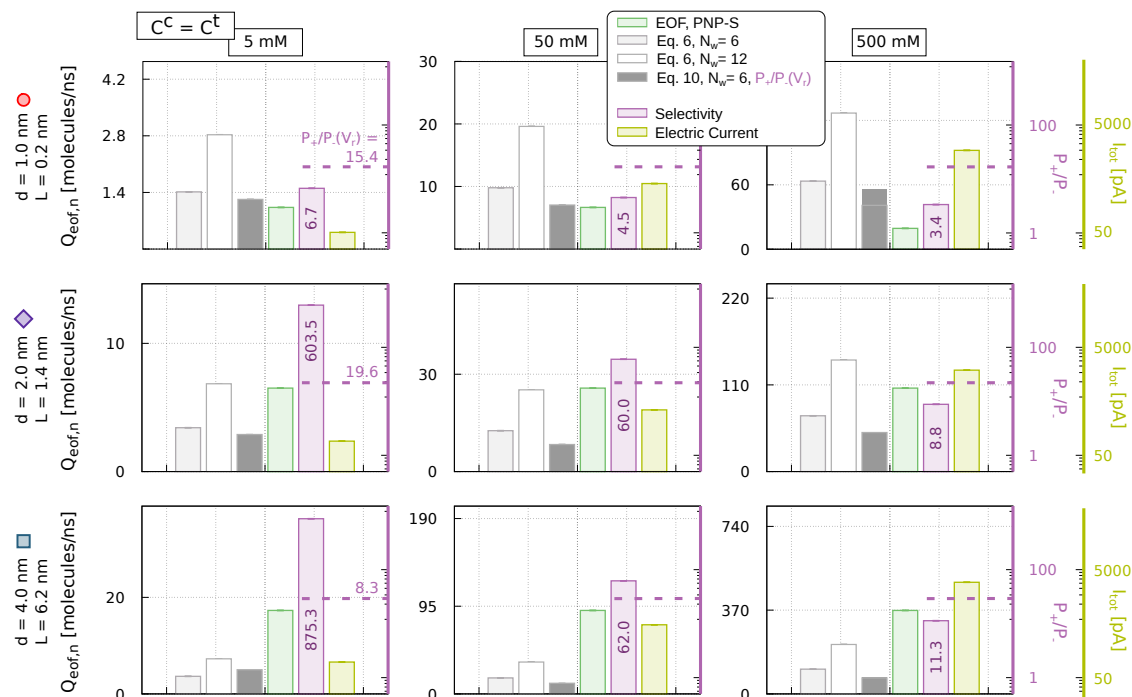


FIG. S7. PNP-S simulations of electrohydrodynamics of systems similar to the the MD ones reported in Fig. S6. In particular, analogous combinations of pore length and diameter are used, as indicated by the labels on the left of each row. Reservoir salt concentration and electric potential is controlled by imposing appropriate boundary conditions at the reservoir hemispherical boundaries, details in Supplementary Figure S2. Panels show the selectivity, total current and EOF from simulations at  $\Delta V = 250$  mV, and EOF predicted from the arguments presented in the main text. Horizontal magenta lines correspond to the selectivity ratio estimated using GHK model, Eq. (4) of the main text, with the  $V_r$  estimated from reversal potential simulations shown in Fig. S5. Dark gray bars refer to EOF from Eq. (10) of the main text using  $P_+/P_-$  estimated from GHK, while white and gray bars refer to estimation using Eq. (6) with different values of  $N_w$ . To compact multiple data on the same plot, three different scales are used for the vertical axis: a linear scale for  $Q_{eof,n}$ , a logarithmic scale for  $P_+/P_-$  and a logarithmic scale for the total current  $I$ . For completeness, the original data are reported in table S1 of the supporting information. Representative voltage, charge and EOF fields are in Supplementary Figure S8.

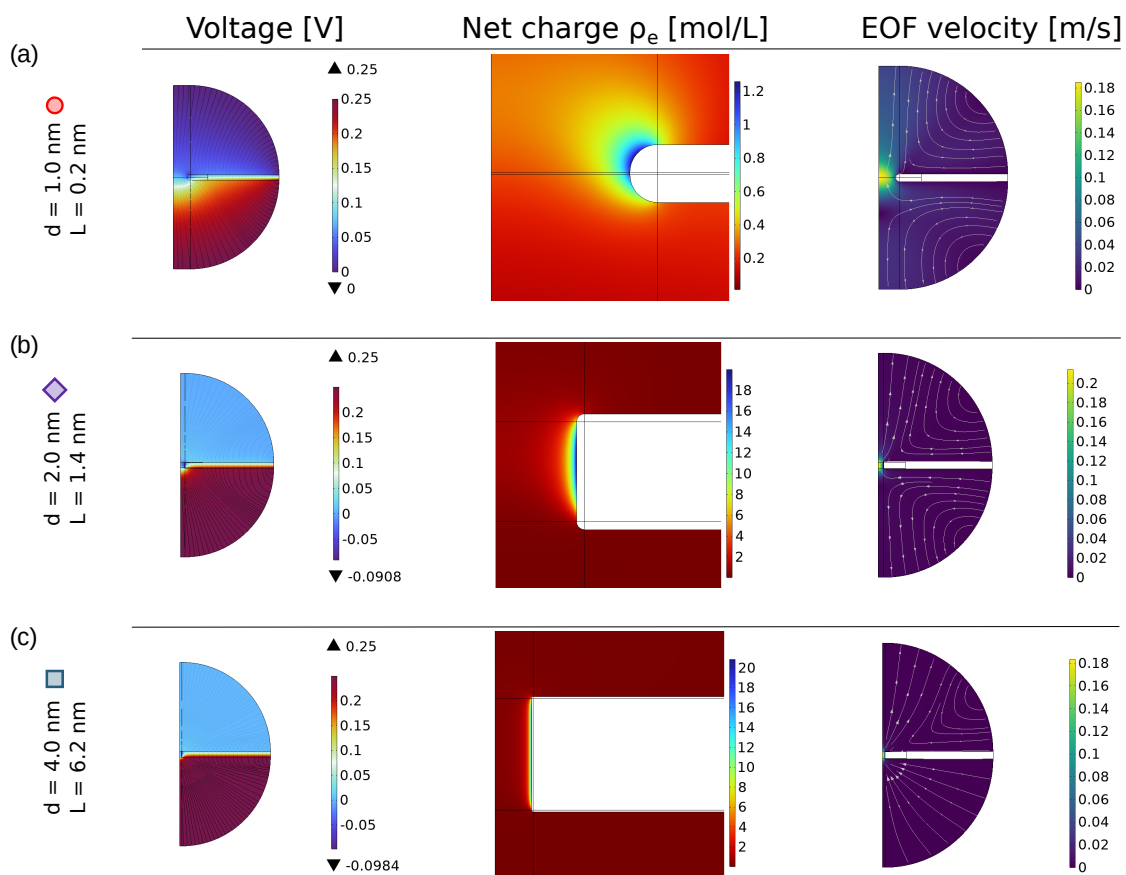


FIG. S8. **Additional PNP-S data.** Representative field distributions of the solution for the data shown in Fig. S7, panel c first column, of the main text, with  $C^c = C^t = 5$  mM. Each panel shows the voltage distribution, net charge density  $\rho_e$  [mol/L], and EOF velocity [m/s] for different nanopore geometries. Pore sizes are shown on the left: (a) Diameter  $d = 1.0$  nm, Length  $L = 0.2$  nm; (b) Diameter  $d = 2.0$  nm, Length  $L = 1.4$  nm; (c) Diameter  $d = 4.0$  nm, Length  $L = 6.2$  nm.

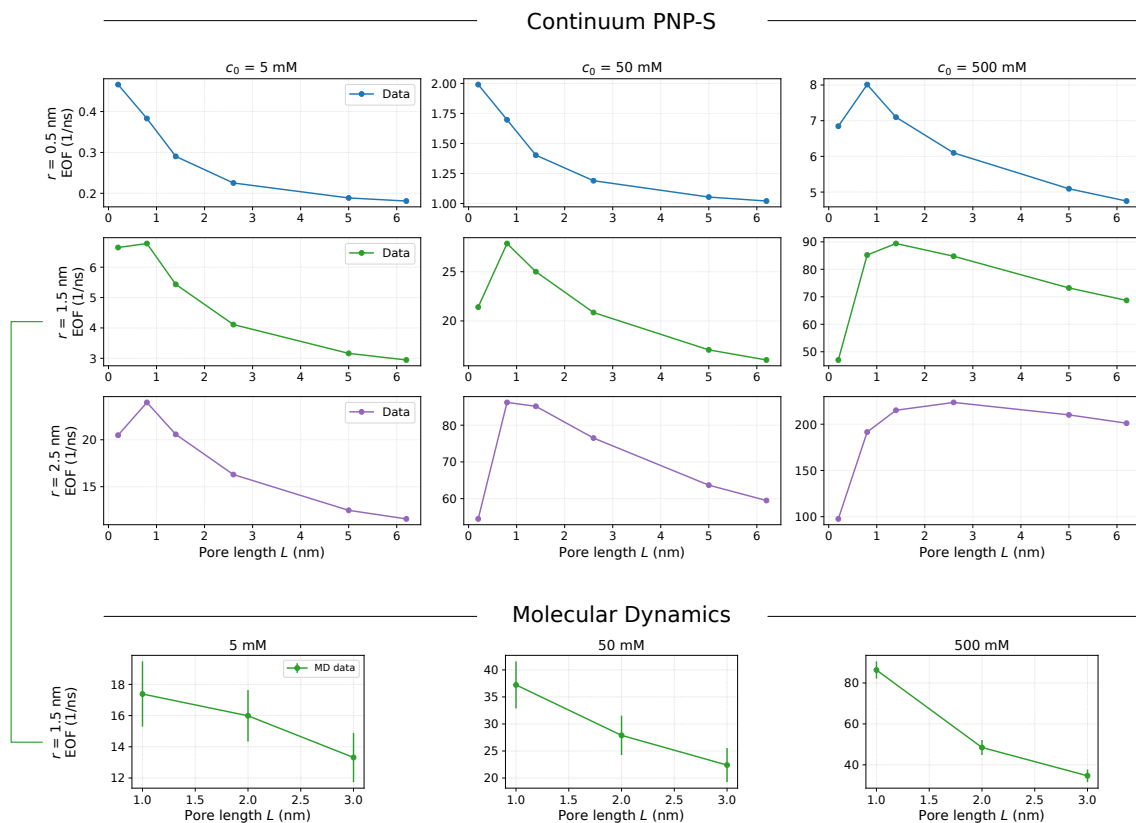


FIG. S9. **Additional data, EOF vs pore length.** Electro-osmotic flow (EOF) as a function of pore length  $L$  for three fixed pore radii ( $r = 0.5, 1.5, 2.5$  nm; rows) and three salt concentrations ( $c_0 = 5, 50, 500$  mM; columns), computed from PNP-S simulations at  $\Delta V = 150$  mV. Bottom panels report some analogous cases, computed by molecular dynamics simulations, for the radius  $r = 1.5$  nm. MD production data are averaged over 400, 200, 100 ns for the 5, 50, 500 mM systems, respectively. Data for the simulated currents and flows are reported in Table S3. In general, MD and PNP-S show similar trends (for instance, the flow overall decreases with the pore length  $L$ ) although some qualitative and quantitative differences are evident. For instance, in the 500 mM case MD predicts a monotonously decreasing EOF while PNP-S shows a maximum around  $L = 1.5$  nm. Systematic comparison between MD and PNP-S is not the aim of our work, nevertheless, we would like to report the possible causes of the different prediction typically reported in the literature. The first point to stress is that PNP-S does not include purely nanoscale effects as liquid slippage and finite size of the ions and, consequently, a quantitative match is not expected unless PNP-S is modified to include these aspects in an effective way (for instance, as boundary condition for slippage or as additional terms for the finite size [S26]). Another difference is that in PNP-S the reservoirs are large somehow emulating the experimental conditions of nanopore sensing devices. This can be done because in finite elements simulations we can use a not uniform computational grid with larger cells far from the pore. Consequently, simulation of large reservoirs is not extremely demanding. Instead, the MD simulations are tri-periodic. In essence, MD does not reproduce a single pore but an infinite array of pores and, consequently, pore-pore interactions can alter the transport properties with respect to the single pore case [S25, S27].

d [nm]	L [nm]	Salt 1:1	$I$ [nA]	$I^+$ [nA]	$I^-$ [nA]	$Q_{eo,n}$ [molecules/ns]
1	0.2	0.005M	0.0592	0.0443	0.0066	1.03
1	0.2	0.05M	0.409	0.336	0.0743	6.66
1	0.2	0.5M	3.124	2.408	0.717	19.43
2	1.4	0.005M	0.0916	0.0915	0.0002	6.51
2	1.4	0.05M	0.347	0.3416	0.0057	25.72
2	1.4	0.5M	2.371	2.129	0.242	105.88
4	6.2	0.005M KCl	0.0972	0.0971	0.0001	17.29
4	6.2	0.05M KCl	0.476	0.468	0.0076	90.43
4	6.2	0.5M KCl	3.378	3.196	0.282	368.73

TABLE S1. PNP-S data for ionic and electroosmotic flow at 250 mV. Data refer to the nanopore systems shown in Fig. S7.  $d$  is the pore diameter, while  $L$  the pore length. The electrolyte is a 1:1 salt water solution, with the two ionic species having opposite charges  $\pm 1e$  and diffusion coefficients  $D_+ = D_- = 2 \times 10^{-9} \text{ m}^2/\text{s}$ . The fluid dynamic viscosity is  $1 \times 10^{-3} \text{ Pa} \cdot \text{s}$  and density  $1000 \text{ kg}/\text{m}^3$ .

d [nm]	L [nm]	Salt	$I$ [nA]	$I^+$ [nA]	$I^-$ [nA]	$Q_{eo,n}$ [molecules/ns]
1	0.5	0.005M KCl	$0.0530 \pm 0.0027$	$0.0443 \pm 0.0025$	$0.0087 \pm 0.0012$	$3.7 \pm 1.4$
1	0.5	0.05M KCl	$0.1125 \pm 0.0039$	$0.0860 \pm 0.0032$	$0.0264 \pm 0.0021$	$6.3 \pm 1.6$
1	0.5	0.5M KCl	$0.787 \pm 0.017$	$0.551 \pm 0.012$	$0.2266 \pm 0.0096$	$25.7 \pm 1.6$
2	1.5	0.005M KCl	$0.1732 \pm 0.0056$	$0.1721 \pm 0.0055$	$0.00103 \pm 0.00078$	$24.1 \pm 2.2$
2	1.5	0.05M KCl	$0.4565 \pm 0.0067$	$0.4464 \pm 0.0078$	$0.0101 \pm 0.0035$	$44.6 \pm 2.4$
2	1.5	0.5M KCl	$2.502 \pm 0.020$	$2.276 \pm 0.032$	$0.226 \pm 0.021$	$171.8 \pm 4.9$
4	6	0.005M KCl	$0.2940 \pm 0.0066$	$0.2765 \pm 0.0065$	$0.0175 \pm 0.0018$	$55.7 \pm 6.0$
4	6	0.05M KCl	$1.016 \pm 0.011$	$0.912 \pm 0.011$	$0.1045 \pm 0.0061$	$150.0 \pm 5.1$
4	6	0.5M KCl	$4.237 \pm 0.025$	$3.231 \pm 0.033$	$1.006 \pm 0.026$	$195.6 \pm 8.3$

TABLE S2. Solid state nanopore data for ionic and electroosmotic flow at 250 mV. Data refer to the nanopore systems shown in Fig. S6.  $d$  is the pore diameter, while  $L$  the pore length.

$d$ [nm]	$L$ [nm]	KCl [M]	$I$ [nA]	$I^+$ [nA]	$I^-$ [nA]	$Q_{eo,n}$ [molecules/ns]
3.0	10.	0.005	$0.167 \pm 0.010$	$0.160 \pm 0.009$	$0.007 \pm 0.004$	$17.3 \pm 2.1$
3.0	20.	0.005	$0.203 \pm 0.010$	$0.195 \pm 0.009$	$0.007 \pm 0.003$	$15.9 \pm 1.6$
3.0	30.	0.005	$0.165 \pm 0.011$	$0.162 \pm 0.011$	$0.003 \pm 0.003$	$13.3 \pm 1.6$
3.0	10.	0.05	$0.421 \pm 0.017$	$0.405 \pm 0.014$	$0.015 \pm 0.010$	$37.2 \pm 4.3$
3.0	20.	0.05	$0.407 \pm 0.016$	$0.377 \pm 0.014$	$0.031 \pm 0.008$	$27.8 \pm 3.6$
3.0	30.	0.05	$0.400 \pm 0.018$	$0.380 \pm 0.016$	$0.020 \pm 0.008$	$22.3 \pm 3.1$
3.0	10.	0.5	$1.523 \pm 0.024$	$1.302 \pm 0.030$	$0.221 \pm 0.027$	$86.3 \pm 4.2$
3.0	20.	0.5	$0.957 \pm 0.021$	$0.877 \pm 0.028$	$0.080 \pm 0.023$	$48.4 \pm 3.6$
3.0	30.	0.5	$0.705 \pm 0.019$	$0.725 \pm 0.025$	$-0.019 \pm 0.018$	$34.6 \pm 3.1$

TABLE S3. Solid state nanopore data for ionic and electroosmotic flow at 150 mV, for different pore lengths. Data refer to the plot shown in Supplementary Fig. S9.  $d$  is the pore diameter, while  $L$  the pore length.

Pore	Salt	$I$ [nA]	$I^+$ [nA]	$I^-$ [nA]	$Q_{eo,n}$ [molecules/ns]
MspA	1M KCl	$1.838 \pm 0.029$	$1.500 \pm 0.045$	$0.338 \pm 0.043$	$43.8 \pm 3.5$
MspA-M3	1M KCl	$1.077 \pm 0.029$	$0.285 \pm 0.042$	$0.791 \pm 0.044$	$-37.7 \pm 3.6$
CytK-2E4D	1M KCl	$0.889 \pm 0.014$	$0.733 \pm 0.026$	$0.156 \pm 0.017$	$21.7 \pm 1.6$
CytK-6K	1M KCl	$0.517 \pm 0.023$	$0.027 \pm 0.007$	$0.490 \pm 0.020$	$-20.4 \pm 0.8$
CsgG-3K	0.5M KCl	$0.441 \pm 0.019$	$0.062 \pm 0.038$	$0.379 \pm 0.038$	$-17.6 \pm 3.7$
CsgG-3K2S	0.5M KCl	$1.010 \pm 0.029$	$0.314 \pm 0.029$	$0.696 \pm 0.036$	$-38.8 \pm 4.9$

TABLE S4. Biological nanopore data for ionic and electroosmotic flow at 250 mV. Data refer to the nanopore systems shown in Fig. 4 and 5 of the manuscript.

## SUPPLEMENTARY REFERENCES

- [S1] David E Goldman. Potential, impedance, and rectification in membranes. The Journal of general physiology, 27(1):37–60, 1943.
- [S2] Alan L Hodgkin and Bernard Katz. The effect of sodium ions on the electrical activity of the giant axon of the squid. The Journal of physiology, 108(1):37, 1949.
- [S3] Yoav Green. The goldman-hodgkins-katz equation, reverse-electrodialysis, and everything in between. arXiv preprint arXiv:2411.03342, 2024.
- [S4] Sabine Straathof, Giovanni Di Muccio, Maaruthy Yelleswarapu, Melissa Alzate Banguero, Carsten Wloka, Nieck Jordy van der Heide, Mauro Chinappi, and Giovanni Maglia. Protein sizing with 15 nm conical biological nanopore yaxab. ACS nano, 17(14):13685–13699, 2023.
- [S5] Li-Qun Gu, Stephen Cheley, and Hagan Bayley. Electroosmotic enhancement of the binding of a neutral molecule to a transmembrane pore. Proceedings of the National Academy of Sciences, 100(26):15498–15503, 2003.
- [S6] Gang Huang, Kherim Willems, Misha Soskine, Carsten Wloka, and Giovanni Maglia. Electro-osmotic capture and ionic discrimination of peptide and protein biomarkers with frac nanopores. Nature communications, 8(1):935, 2017.
- [S7] Alina Asandei, Irina Schiopu, Mauro Chinappi, Chang Ho Seo, Yoonkyung Park, and Tudor Luchian. Electroosmotic trap against the electrophoretic force near a protein nanopore reveals peptide dynamics during capture and translocation. ACS applied materials & interfaces, 8(20):13166–13179, 2016.
- [S8] Matteo Baldelli, Giovanni Di Muccio, Adina Sauciuc, Blasco Morozzo della Rocca, Francesco Viola, Sébastien Balme, Andrea Bonini, Giovanni Maglia, and Mauro Chinappi. Controlling electroosmosis in nanopores without altering the nanopore sensing region. Advanced Materials, page 2401761, 2024.
- [S9] James C Phillips, Rosemary Braun, Wei Wang, James Gumbart, Emad Tajkhorshid, Elizabeth Villa, Christophe Chipot, Robert D Skeel, Laxmikant Kale, and Klaus Schulten. Scalable molecular dynamics with namd. Journal of computational chemistry, 26(16):1781–1802, 2005.
- [S10] Ulrich Essmann, Lalith Perera, Max L Berkowitz, Tom Darden, Hsing Lee, and Lee G Pedersen. A smooth particle mesh ewald method. The Journal of chemical physics, 103(19):8577–8593, 1995.
- [S11] Bernard R Brooks, Charles L Brooks III, Alexander D Mackerell Jr, Lennart Nilsson, Robert J Petrella, Benoît Roux, Youngdo Won, Georgios Archontis, Christian Bartels, Stefan Boresch, et al. Charmm: the biomolecular simulation program. Journal of computational chemistry, 30(10):1545–1614, 2009.
- [S12] William L Jorgensen, Jayaraman Chandrasekhar, Jeffrey D Madura, Roger W Impey, and Michael L Klein. Comparison of simple potential functions for simulating liquid water. The Journal of chemical physics, 79(2):926–935, 1983.
- [S13] Jejoong Yoo and Aleksei Aksimentiev. Improved parametrization of li+, na+, k+, and mg2+ ions for all-atom molecular dynamics simulations of nucleic acid systems. The journal of physical chemistry letters, 3(1):45–50, 2012.
- [S14] Glenn J Martyna, Douglas J Tobias, and Michael L Klein. Constant pressure molecular dynamics algorithms. The Journal of chemical physics, 101(5):4177–4189, 1994.
- [S15] Giovanni Di Muccio, Blasco Morozzo della Rocca, and Mauro Chinappi. Geometrically induced selectivity and unidirectional electroosmosis in uncharged nanopores. ACS nano, 16(6):8716–8728, 2022.
- [S16] Aleksij Aksimentiev and Klaus Schulten. Imaging  $\alpha$ -hemolysin with molecular dynamics: ionic conductance, osmotic permeability, and the electrostatic potential map. Biophysical journal, 88(6):3745–3761, 2005.
- [S17] Emma Letizia Bonome, Fabio Cecconi, and Mauro Chinappi. Electroosmotic flow through an  $\alpha$ -hemolysin nanopore. Microfluidics and Nanofluidics, 21(5):96, 2017.
- [S18] Adina Sauciuc, Blasco Morozzo della Rocca, Matthijs Jonathan Tadema, Mauro Chinappi, and Giovanni Maglia. Translocation of linearized full-length proteins through an engineered nanopore under opposing electrophoretic force. Nature Biotechnology, pages 1–7, 2023.
- [S19] Michael Faller, Michael Niederweis, and Georg E Schulz. The structure of a mycobacterial outer-membrane channel. Science, 303(5661):1189–1192, 2004.
- [S20] Mikhail A Lomize, Andrei L Lomize, Irina D Pogozheva, and Henry I Mosberg. Opm: orientations of proteins in membranes database. Bioinformatics, 22(5):623–625, 2006.
- [S21] Parveen Goyal, Petya V Krasteva, Nani Van Gerven, Francesca Gubellini, Imke Van den Broeck, Anas-

- tassia Trounpiotis-Tsaïlaki, Wim Jonckheere, Gérard Péhau-Arnaudet, Jerome S Pinkner, Matthew R Chapman, et al. Structural and mechanistic insights into the bacterial amyloid secretion channel csgg. Nature, 516(7530):250, 2014.
- [S22] Torsten Schwede, Jurgen Kopp, Nicolas Guex, and Manuel C Peitsch. Swiss-model: an automated protein homology-modeling server. Nucleic acids research, 31(13):3381–3385, 2003.
- [S23] William Humphrey, Andrew Dalke, Klaus Schulten, et al. Vmd: visual molecular dynamics. Journal of molecular graphics, 14(1):33–38, 1996.
- [S24] Paul S Crozier, Douglas Henderson, Richard L Rowley, and David D Busath. Model channel ion currents in nacl-extended simple point charge water solution with applied-field molecular dynamics. Biophysical journal, 81(6):3077–3089, 2001.
- [S25] Matteo Baldelli, Giovanni Di Muccio, Francesco Viola, Alberto Giacomello, Fabio Cecconi, Sébastien Balme, and Mauro Chinappi. Performance of single nanopore and multi-pore membranes for blue energy. ChemPhysChem, page e202400395, 2024.
- [S26] Alberto Gubbiotti, Matteo Baldelli, Giovanni Di Muccio, Paolo Malgaretti, Sophie Marbach, and Mauro Chinappi. Electroosmosis in nanopores: computational methods and technological applications. Advances in Physics: X, 7(1):2036638, 2022.
- [S27] A Gadaleta, C Sempere, Simon Gravelle, Alessandro Siria, R Fulcrand, C Ybert, and Lydéric Bocquet. Sub-additive ionic transport across arrays of solid-state nanopores. Physics of Fluids, 26(1), 2014.